ACS Photonics

Article

Cite This: ACS Photonics 2018, 5, 2816−2824

Controlling the Plasmonic Properties of Ultrathin TiN Films at the Atomic Level

Deesha Shah,[†] Alessandra Catellani,[‡] Harsha Reddy,[†] Nathaniel Kinsey,[§] Vladimir Shalaev,[†] Alexandra Boltasseva,[†] and Arrigo Calzolari*[,‡]

[†]School of Electrical and Computer Engineering and Birck Nanotechnology Center, Purdue University, West Lafayette, Indiana 47907, United States

[‡]CNR-NANO Istituto Nanoscienze, Centro S3, I-41125 Modena, Italy

[§]School of Electrical and Computer Engineering, Virginia Commonwealth University, Richmond, Virginia 23220, United States

Supporting Information

ABSTRACT: By combining first-principles theoretical calculations and experimental optical and structural characterization such as spectroscopic ellipsometry, X-ray spectroscopy, and electron microscopy, we study the dielectric permittivity and plasmonic properties of ultrathin TiN films at an atomistic level. Our theoretical results indicate a remarkably persistent metallic character of ultrathin TiN films and a progressive red shift of the plasmon energy as the thickness of the film is reduced, which is consistent with previous experimental studies. The microscopic origin of this trend is interpreted in terms of the characteristic two-band electronic structure of the system. Surface oxidation and substrate strain are also investigated to explain the deviation of the optical properties from the ideal case. This paves the way to the realization of ultrathin TiN films with tailorable and tunable plasmonic properties in the visible range for applications in ultrathin metasurfaces and nonlinear optics.

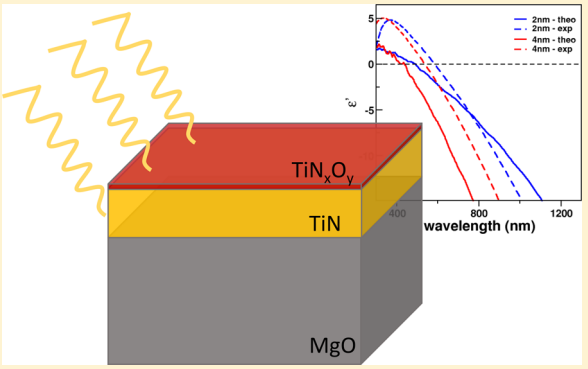

KEYWORDS: *plasmonics, optical properties, DFT, ellipsometry, titanium nitride, ultrathin films*

Downloaded via CNR on July 19, 2018 at 08:26:02 (UTC).
See https://pubs.acs.org/sharingguidelines for options on how to legitimately share published articles.

Recent developments in nanofabrication techniques have facilitated a surge of nanoplasmonic devices whose properties can be engineered by careful structural control of their metallic building blocks.[1] The usage of plasmonic materials, mostly metals, that support the light-coupled subwavelength oscillations of free electron clouds has led to advances in various applications, such as sensing,[2−4] photovoltaics,[5−7] and optical circuitry,[8,9] unachievable with conventional dielectric photonic materials. Along with the control of the lateral dimensions of plasmonic structures, it is also possible to tailor the properties by adjusting the thickness of plasmonic materials, all the way down to a few monolayers.[10,11] As the dimensions shrink down to nanometer range thicknesses, quantum phenomena emerge as a result of the strong electron confinement, making ultrathin plasmonic materials ideal platforms to study light−matter interactions at the nanoscale.[12,13] For example, the strong confinement leads to an enhanced nonlinear optical response in ultrathin films in comparison to their bulk counterparts.[14,15] Most importantly, ultrathin plasmonic films are predicted to have a greatly increased sensitivity to the local dielectric environment, strain, and external perturbations.[10] Consequently, unlike conventional metals with properties that are challenging to tailor, atomically thin plasmonic materials exhibit optical responses that can be engineered by precise control of their thickness, composition, and the electronic and structural properties of the substrate and superstrate.[10,16,17] This unique tailorability, unachievable with bulk or relatively thick metallic layers, establishes ultrathin plasmonic films as an attractive material platform for the design of tunable and dynamically switchable metasurfaces.[18] In order to realize these applications, a deeper insight into plasmonic material properties at the nanoscale is required.

To investigate the sought after atomically thin plasmonic regime, there have been several efforts to grow ultrathin (<10 nm) metallic films with various plasmonic materials, such as gold[19] and titanium nitride (TiN).[11,20] For noble metals, which are the usual choice of material for plasmonic structures, the deposition of smooth, continuous ultrathin films is very challenging due to island formation and large defect concentrations.[19,21] In contrast, the epitaxial growth of TiN on lattice-matched substrates, such as MgO, allows for the growth of plasmonic thin films with thicknesses down to 2 nm.[22,23] Due to its high quality growth, chemical stability, and tailorable optical properties, TiN is the ideal material choice to

Received: December 17, 2017
Published: May 11, 2018

© 2018 American Chemical Society

DOI: 10.1021/acsphotonics.7b01553
ACS Photonics 2018, 5, 2816−2824

study plasmonic properties at the atomic level. The electronic, optical, and mechanical properties of TiN single or polycrystalline bulk system and thick films (>100 nm) have been largely studied[24−28] using several experimental and theoretical techniques, including spectroscopic ellipsometry,[29,30] X-ray, UV photoemission and Auger spectroscopy,[31,32] electron energy loss,[33,34] Hall electron transport,[35] scanning electron and tunneling microscopies,[36,37] and tight-binding and ab initio simulations.[24,38−40]

On the contrary, even though a few reports on growth[41,42] and electron transport[43,44] appeared in the last years, the optical properties of ultrathin TiN films (<10 nm) are still largely unexplored. In particular, while the retention and manipulation of optical properties in ultrathin TiN films has been recently demonstrated,[11,18] a comprehensive investigation of the underlying physics affecting the plasmonic properties in ultrathin metal films is still lacking. Hence, to move toward the realization of practical devices utilizing ultrathin plasmonic materials, additional studies are needed to understand the optical behavior of ultrathin films and the different factors contributing to their thickness dependent properties. In this study, we present a joint theoretical−experimental study on the plasmonic properties of ultrathin TiN films. Structural and compositional characterization of the films provide further insight into the possible avenues to tailor the optical response. We show that the effects of oxidation and strain on the optoelectronic and plasmonic properties of the thin films emerge as fundamental parameters to optimize the nanostructure response.

METHOD

Theory. First-principles density functional (DFT) calculations are carried out with semilocal (PBE[45]) exchange-correlation functional, using plane wave basis set (with a cutoff energy of 200 Ry) and norm-converging pseudopotentials,[46] as implemented in Quantum Espresso[47] codes. A uniform (28 × 28) k-point grid is used for summations over the 2D Brillouin zone.

Extended TiN films are simulated using periodically repeated supercells. Each unit cell (4.24 × 4.24 × 55.00) Å^3 has a ($\sqrt{2}$ x $\sqrt{2}$) 2D lateral periodicity and contains 1−10, 15, and 20 layers of TiN(001), as shown in Figure 1a. The lattice parameter of TiN surface (4.24 Å) is obtained from the optimization of the corresponding bulk crystal.[40] When considering the effect of oxidation, O adatoms are symmetrically adsorbed on each surface to avoid a spurious dipolar field across the cell. To avoid interaction between adjacent slab replicas, these are separated by at least 15.0 Å of vacuum. Each structure is fully relaxed until forces on all atoms become lower than 0.03 eV/Å.

The complex dielectric function $\hat{\varepsilon} = \varepsilon' + i\varepsilon''$ is evaluated using the code epsilon.x, also included in the Quantum ESPRESSO suite. This code implements an independent particle formulation of the frequency-dependent (ω) Drude−Lorentz model for solids:[48,49]

$$\hat{\varepsilon}(\omega) = \varepsilon' + i\varepsilon'' = 1 - \sum_{k,n} f_k^{n,n} \frac{\omega_p^2}{\omega^2 + i\eta\omega} + \sum_{k,n\neq n'} f_k^{n,n'} \frac{\omega_p^2}{\omega_{k,n,n'}^2 - \omega^2 - i\gamma\omega} \quad (1)$$

where $\omega_p = \sqrt{e^2 n_e/\varepsilon_0 m^*}$ is the bulk plasma frequency, e is the electron charge, n_e the electron density, ε_0 is the dielectric permittivity of vacuum, and m^* the electron effective mass. $\hbar\omega_{k,n,n'} = E_{k,n'} - E_{k,n}$ are the vertical band-to-band transition energies between occupied and empty Bloch states, labeled by the quantum numbers ($\boldsymbol{k}$, n) and ($\boldsymbol{k}$, n'), respectively. $f_k^{n,n}$ and $f_k^{n,n'}$ are the oscillator strengths for the Drude and Lorentz parts and are related to the dipole matrix elements between Bloch states. η and γ are the Drude-like and Lorentz-like relaxation terms, which account for the finite lifetime of the electronic excitations and implicitly include the effects of the dissipative scattering. The capability of the present approach in simulating the optical properties of plasmonic materials has been extensively proved in refs 40, 49, and 50. As a further accuracy test, we report in the Supporting Information (SI) the comparison between the dielectric function of TiN bulk (B_1 phase) calculated with Drude-Lorentz approach and with the one based on Time-Dependent Density Functional Perturbation Theory, adopted in ref 40 and compared with experiments.

The free carrier density n_e is obtained inverting the Drude-like expression for the plasma frequency, $n_e = \omega_p^2 \varepsilon_0 m^* e^{-2}$. Rigorously, since TiN has a nonspherical Fermi surface with three bands crossing the Fermi energy, m^* is direction and band dependent. On the other hand, it is an experimental custom to assume a single parabolic model and extract an average m^* (usually deriving from optical measurements) to combine it with resistivity measurements in order to estimate the experimental carrier density. For bulk systems the estimated m^* is very close to the free electron mass m_0 ($m^* = 1.1m_0$).[35] For films thicker than 2 nm, the average effective mass is about $1.3m_0$ and it is expected to decrease for thinner films.[11] Direct evaluation from our DFT band structure calculation around Γ point gives $m^* = 0.99m_0$ for bulk and $m^* = 0.9m_0$ for 4L film, respectively, in good agreement with experimental estimates. In the following, for the calculation of n_e, we assumed $m^* = m_0$ for each system, with an error band (orange shaded area, Figure 1) among the extrema $m^* = 0.9−1.3m_0$.

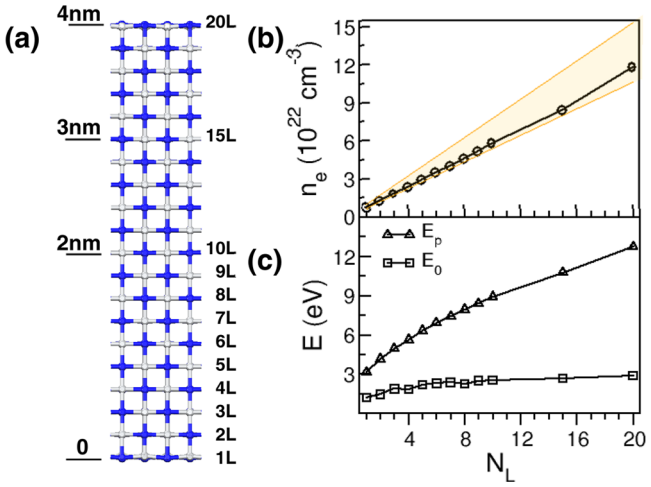

Figure 1. (a) Side view of 1−10, 15, and 20 layer thick TiN(100) slabs used in the simulations. (b) Free electron charge density n_e, and (c) volume-plasmon E_p and screened-plasmon E_0 energies for 1−20 layer films (0−4 nm). Orange shaded area estimate the error band associated with the choice of m^*.

Experiments. Ultrathin TiN films with thicknesses of 2, 4, 6, 8, 10, and 30 nm were grown on MgO using DC reactive magnetron sputtering. The TiN deposition was completed by sputter deposition of a titanium target in a 60% nitrogen and 40% argon environment at 5 mT with 200 W of DC power

DOI: 10.1021/acsphotonics.7b01553
ACS Photonics 2018, 5, 2816−2824

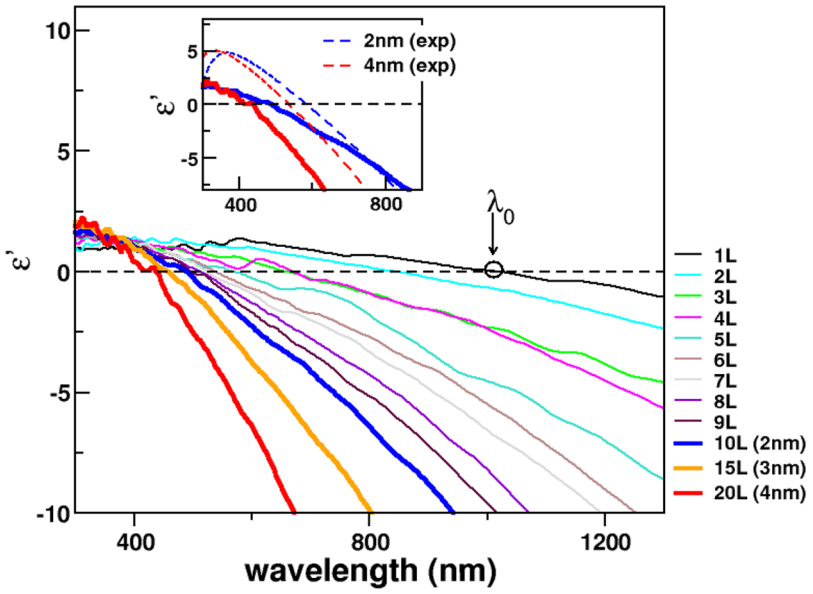

Figure 2. Real part of the dielectric function as a function of the number of layers N_L. Inset shows the comparison between theoretical (thick straight lines) and experimental (thin dashed lines) for 2 (blue) and 4 nm (red) films, respectively.

with the substrate heated to 800 °C, resulting in high quality epitaxial films with low roughness.[11]

The Kratos X-ray photoelectron spectrometer was used for the surface analysis of a 30 nm TiN film. A monochromatic Al Kα (1486.6 eV) X-ray source was used as the incident radiation. The wide scan for the overall spectra is performed with a scanning step of 1000 meV, while the narrow scans for the elemental peaks are performed with a scanning steps of 50 meV. The narrow scans were peak fitted using the CasaXPS software. The spectral energy scale was calibrated with the binding energy of C 1s set to 284.5 eV.

The linear optical properties of the 2, 4, 6, 8, and 10 nm films were measured using variable angle spectroscopic ellipsometry at angles of 50° and 70° for wavelengths from 400 to 2000 nm. A Drude-Lorentz model consisting of one Drude oscillator and one Lorentz oscillator was used to fit the measurements.[11] The charge densities in the TiN films were determined via standard Hall measurements. Using photolithography and dry etching processes, Greek crosses were fabricated from the TiN films, and gold contact pads were applied. The Hall resistance was determined by measuring the voltage across two arms of the cross while a current (10 mA) passing through the other two arms generates an out-of-plane magnetic field, from which the charge density can be calculated.[11]

RESULTS AND DISCUSSION

The optical properties of ultrathin TiN with thicknesses ranging from one to 20 monolayers (0−4 nm) calculated using DFT are summarized in Figures 1 and 2. Figure 1b reports the thickness variation of the free electron density n_e. Figure 1c displays the thickness variation of the volume−plasmon energy $E_p = E(\omega_p)$ and of the screened-plasmon energy $E_0 = E(\omega_0)$, where $\omega_0 = 2\pi c/\lambda_0$, and λ_0 corresponds to the wavelength where the real part (ε') of the dielectric function changes sign [$\varepsilon'(\lambda_0) = 0$]. Figure 2 shows the plots of the ε' function as resulting from the solution of Drude-Lorentz model of eq 1.

All systems exhibit a metallic character and, except for the single layer (1L), have a high carrier density of the order of 10^{22} cm^{-3}, in agreement with the experimental results[11] (Figure S2, SI). Nonetheless, with decreasing thickness, the films become less metallic. The electron density n_e decays almost linearly with the number of layers N_L (Figure 1b) and the real part of the dielectric function (Figure 2) decreases in magnitude as a function of N_L (the imaginary part also decreases, not shown). The latter is an indication of the progressive reduction of the electronic screening in ultrathin layers. Additionally, the crossover wavelength λ_0 red shifts as the thickness decreases. This trend is in qualitative agreement with the experimental results summarized in Figure S2 of SI, where the optical properties of epitaxial ultrathin TiN films with thicknesses of 2, 4, 6, 8, and 10 nm grown on MgO were measured using variable angle spectroscopic ellipsometry.[11] It is important to note that, although the theoretical results cover a smaller range of thicknesses (0−4 nm) and directly compare only with the two thinnest experimental samples (2−4 nm), they are still well representative of the trends showed by the experimental results. This is confirmed also by the $1/N_L$ fit of E_0 displayed in Figure S3 (SI), which shows that, except for 1L−3L systems, all the other results present a linear behavior as the number of layers ($1/N_L$) increases (decreases), and the trends can thus be used to compare with experimental data for thicker films.

At the crossover wavelength λ_0, the imaginary part of the dielectric function ε'' also has a minimum. The condition $\varepsilon(\lambda_0) \approx 0$ corresponds to the possibility of exciting a plasmon-like resonance in the visible range.[40,51,52] The difference between E_p and E_0 for each thickness value (Figure 1c) indicates that the plasmon excitations in the optical range (E_0) do not involve the overall charge density of the system, as for the high energy volume plasmon (E_p), but only a reduced "screened" fraction ($n_e \approx 10^{21}$ cm^{-3}). This is the result of a complex interplay between interband and intraband transitions that effectively screen the amount of free charge that can be collectively excited in the optical range.[40] E_p and E_0 have two evident functional trends as a function of the thickness: E_p varies in the range 3.1−12.7 eV (1L−20L) with an almost ideal square root behavior (i.e., n_e varies linearly with thickness), while E_0 is limited to a much smaller variation range 1.2−2.9 eV for 1−20 layers,

DOI: 10.1021/acsphotonics.7b01553
ACS Photonics 2018, 5, 2816−2824

respectively, due to the interband-transition screening that is active even in ultrathin films (see below). We further note that the value of volume-plasmon for TiN bulk is E_p^{bulk} = 25.4 eV,[33,40] larger than the values resulting in the present case: Despite their metallic character, these films have not yet reached the bulk (or thick film) density limit, remaining well within the ultrathin regime.

The red shift of the crossover wavelength along with the reduction of the real and imaginary parts of the dielectric function when the thickness is reduced perfectly fits with a recent electromagnetic model explicitly developed to describe the confinement effects on the optical properties of ultrathin plasmonic films.[17] Here, taking advantages of first-principles results, we can discuss the effect of quantum confinement in terms of the electronic structure of the ultrathin films. The electron density of states (DOS) of each TiN film close to the Fermi energy (E_F) is characterized by two contiguous groups of bands, labeled **1** and **2** in Figure 3, which shows the DOS

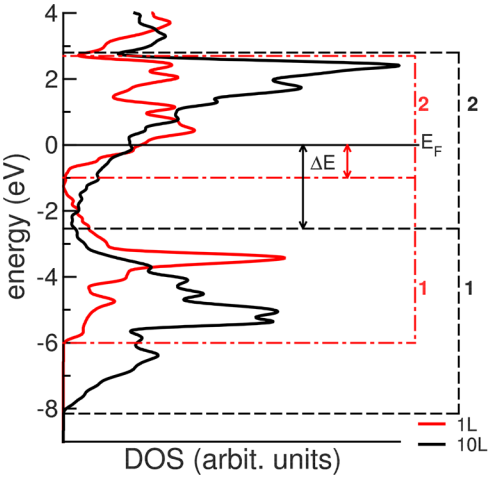

Figure 3. Simulated DOS plots for 1L (red) and 10L (black) systems. Dashed lines remark energy position with respect to the Fermi level (E_F) and the energy width of the two main groups of bands (**1**, **2**) responsible for crossover wavelength in the visible range (λ_0).

spectra for the cases 1L (red) and 10L (black). Bands forming the multiplet **1** have a predominant N(2*p*) character with a minor contribution from Ti(e_g) orbitals, while bands of group **2** mostly derive from Ti(t_{2g}) orbitals slightly hybridized with N(2*p*) states. The plasmonic behavior of TiN originates from intraband transitions of group-**2** bands that cross the Fermi level, giving rise to a Drude-like tail in the real part of the dielectric function and to the high-energy volume plasmon. The excitation of interband **1** → **2** transitions at lower energies gives a positive contribution to the (negative) Drude component of ε' that becomes globally positive at the crossover frequency λ_0. Thus, in a first approximation, the energy position of band **1** with respect to the Fermi level (ΔE in Figure 3) defines the energy of the screened plasmon (E_0). The effect of confinement actually changes the energy width and the energy position of bands **1** and **2** with respect to E_F. Despite the two sets of bands are clearly present in both systems, their characteristics are quite different: with decreasing thickness the surface-to-bulk ratio increases along with the number of under-coordinated surface atoms. The presence of frustrated bonds imparts a shrinking of the bandwidth of bands **1** and **2** (i.e., higher spatial electron localization), and an upshift of occupied bands (i.e., lower binding energies), which results in a decrease of ΔE (i.e., E_0 red-shifts). Thus, despite the same formal electron density, the reduction of thickness increases the surface contribution and the electron localization, giving an effective reduction of the free electron charges.

This qualitatively explains the modifications of the optical properties observed in the experiments varying the film thickness (Figure S2).[11] In order to have a more quantitative comparison, we superimpose the experimental ε' spectrum (inset of Figure 2) for the 2 and 4 nm films. Albeit in qualitative agreement, the theoretical values of λ_0 are systematically blue-shifted with respect to the experimental ones, that is, the crossover wavelength of 2 and 4 nm TiN films are reached at a larger thickness in the experimental studies compared to the theoretical results. In particular, the theoretical value of for the 10L system (i.e., 2 nm), λ_0 = 489 nm (blue straight line), is blue-shifted by 96 nm with respect to the experimental value, λ_0 = 585 nm (blue dashed line). For the 20L system (i.e., 4 nm), λ_0 = 430 nm (red straight line), is blue-shifted by 105 nm with respect to the experimental value, λ_0 = 535 nm (red dashed line).

Two different factors that may originate the λ_0 difference between experiment and theory are considered: (i) surface oxidation and (ii) interface strain.

Typically, a layer of TiN_xO_y of approximately 1−2 nm is formed on the film surface,[53] which would reduce the effective thickness of the films. X-ray photoelectron spectroscopy was conducted on a 30 nm TiN film grown on MgO to study the oxidation mechanisms on the film surface (Figure 4). The N_{1s}, O_{1s}, and Ti_{2p} peaks are decomposed as shown in Figure 4b, c, and d, respectively. Three peaks can be used to fit the N_{1s} spectrum, where the dominant peak at 396.8 eV is attributed to Ti−N bonds. The peak at 397.7 eV is due to the formation of an oxynitride compound, resulting in Ti−O−N bonds.[54,55] An additional weak peak in the fitting is observed at a lower energy 395.8, which may be the result of other impurities or nitrogen chemically bonded on the surface.[55,56] While evidence of TiN_xO_y is also present in the O_{1s} spectrum (531.2 eV), the main peak at 529.9 eV is indicative of the existence of Ti−O bonds in the films.[57] These results are also corroborated by the decomposition of the Ti_{2p} peak using three pairs of doublets (2p 1/2 and 2p 3/2) for Ti−N, Ti−N−O, and Ti−O,[57,58] implying that the films are systems consisting of TiN, TiN_xO_y, and TiO_2. The binding energies and shapes of the peaks in Figure 4 are consistent with those reported in literature.[54,55,57,58]

To determine how the different oxidation phases possibly modify the optical properties, nine different configurations of an oxide capping layer on a 2 nm thick film are considered. These include oxygen atoms in N substitutional sites (O_N), single oxygen (O_s) and O_2 molecules adsorbed on the surface (Figure 5a), and their combination. The corresponding ε' plots are collected in panels (b) and (c). The dielectric function of ideal 2 nm thick layer (i.e., 10L, black thick line) and the corresponding experimental results (black dashed line) are included for comparison.

Since the metallic bands at the Fermi level are mainly due to Ti-derived states, the coordination of Ti atoms is crucial in the resulting optoelectronic properties of the system. If a single or a few O atoms substitute surface nitrogens, this does not substantially change the Ti coordination leaving the electronic structure almost unchanged (Figure 5b). Rather, O_N is an aliovalent impurity that acts as an n-type dopant, which

DOI: 10.1021/acsphotonics.7b01553
ACS Photonics 2018, 5, 2816−2824

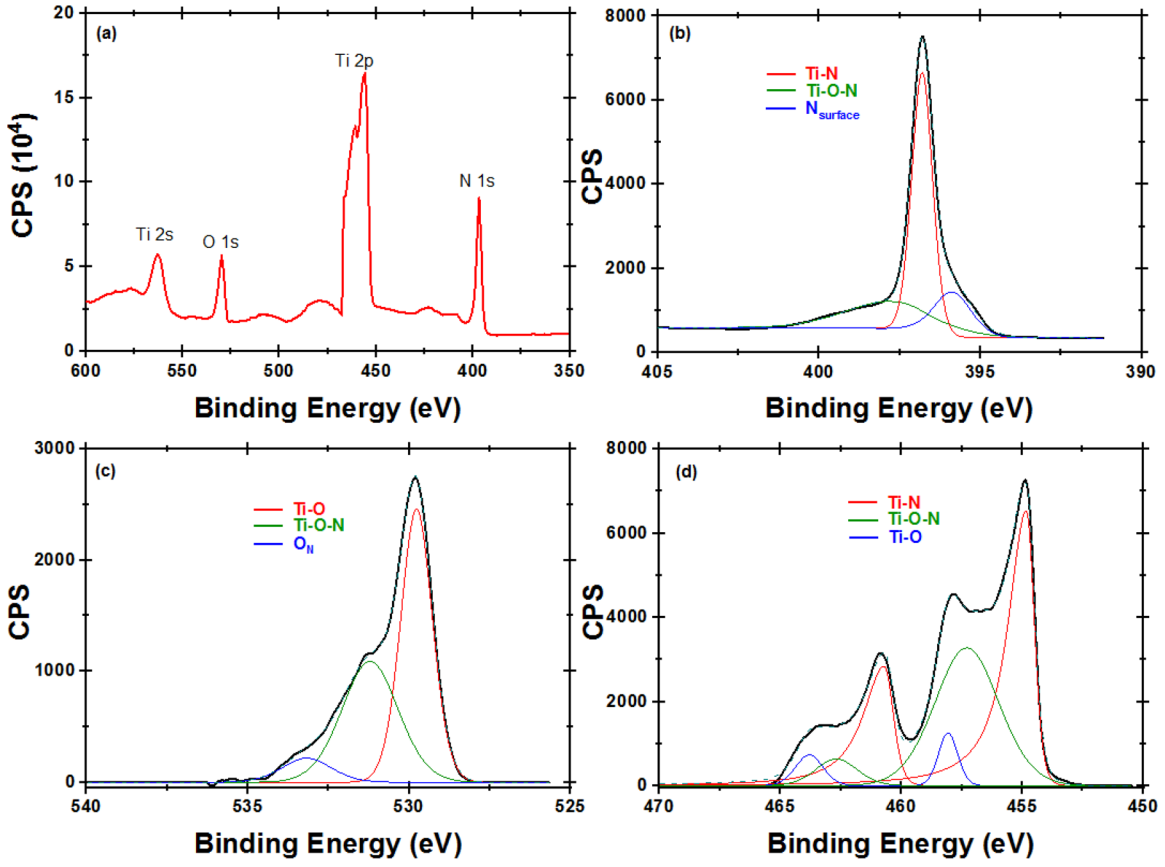

Figure 4. (a) XPS spectrum of a partially oxidized 30 nm TiN film grown on MgO by DC magnetron sputtering. The (b) N_{1s}, (c) O_{1s}, and (d) Ti_{2p} peaks are fitted to determine the local chemical environment. CPS are the counts per second collected at each energy. The black curve represents the actual XPS data collected, while the blue dashed curve is the generated envelope curve from peak fitting.

increases the electron density. Consequently, a blue shift in the crossover wavelength is observed, contrary to experimental results. Conversely, single oxygen atoms on the surface have little effect on the optical properties (Figure 5b). On the contrary, O_2 molecules do cause a red shift of the crossover wavelength, tending toward the experimental value (Figure 5c). The O_2 molecules change the coordination of the Ti atoms on the surface to resemble the configuration for TiO_2. As the amount of oxygen is increased, surface Ti easily coordinates with oxygen forming Ti−O bonds at the surface, reducing the overall thickness of pure TiN and leading to the slower blue shift of the crossover wavelengths observed experimentally. To prove this statement we consider, as key example, the case where $3O_N$ and $2O_2$ are included in the system (labeled $3O_N + 2O_2$, Figure 6). After atomic relaxation, the surface layer displays a remarkable structural rearrangement, where the Ti atoms may have three different kinds of coordination: (i) a partially detached oxide layer forms on the surface, where Ti is bonded to O atoms only. This is in agreement with the Ti−O feature revealed in the XPS data (Figure 4c). (ii) In the central region of the slab, Ti is 6-fold coordinated with N and forms the TiN core of the film (see also the main peak in Figure 4b). (iii) In the intermediate region N and O coexist and Ti atoms are coordinated with both species, giving rise to mixed Ti−N−O phases. This is coherent with the appearance of Ti−N−O features in N_{1s} and O_{1s} spectra.

The effects on the electronic structure are evident in Figure 6b, where the comparison with the DOS of ideal 10L system is presented. The total DOS of $3O_N+2O_2$ system is reminiscent of the original bands **1** - **2** and the system maintains a metallic character, but the presence of oxygen (shaded area) includes new localized states across the Fermi level. This has a 2-fold effect: first, it reduces the effective thickness of TiN; second, it introduces further O-derived states that contribute to interband transitions, further shifting the crossover wavelength toward red. The oxide layer, however, is not sufficiently thick to exhibit the characteristic dielectric features of TiO_2. Although the exact microscopic reconstruction of the surface strictly depends on the growth process, this example is sufficient to give optical properties in quantitative agreement with experimental findings (Figure 5b).

Since experimental TiN samples are not free-standing but grown on MgO substrate, the effect of a substrate induced strain is included in the simulations and compared to experiments. The lattice mismatch would introduce a strain in the film, changing the in-plane lattice parameter of TiN. In order to investigate this effect without including other structural modifications derived by the explicit description of the substrate, we simulated a set of free-standing 10-layer-thick TiN films with varying in-plane lattice constants, which span the range [−3% to +6%] with respect to the equilibrium lattice parameter (a_0^{TiN} = 4.24 Å), as shown in Figure 7. As the lattice parameter is reduced (compressive strain), the crossover wavelength blue shifts; the opposite happens when the lattice parameter is increased (tensile strain). To reach the experimental value for the crossover wavelength, a tensile strain of ∼6% is required. Although ultrathin films may sustain large amounts of strain due to interface mismatch, the latter

DOI: 10.1021/acsphotonics.7b01553
ACS Photonics 2018, 5, 2816−2824

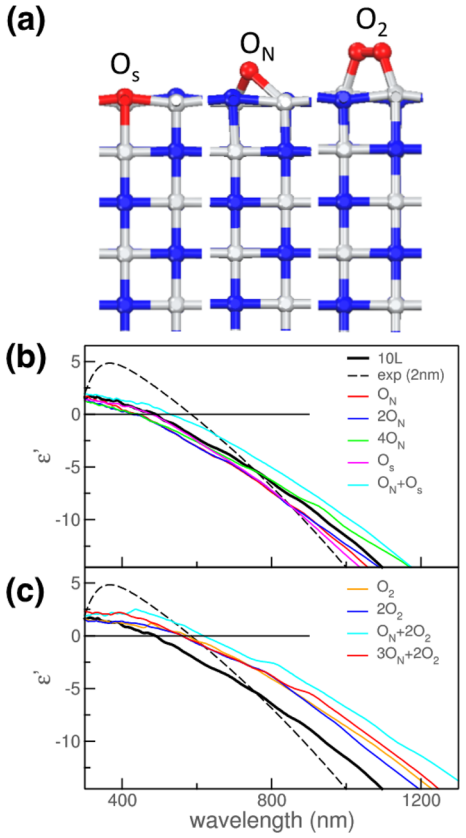

Figure 5. (a) Configurations for single oxygen atom in a nitrogen substitutional site (O_N), single oxygen atom on the surface (O_s) or diatomic oxygen molecule on the film surface (O_2). Real part of the dielectric function of oxidized TiN film including (b) single atoms O_N and O_s and (c) O_2 molecule. Different combinations of these three main configurations are modeled to determine the effect of oxygen in the films. Theoretical ideal model (10L) and the corresponding experimental spectra are reported in panels (b) and (c) for direct comparison.

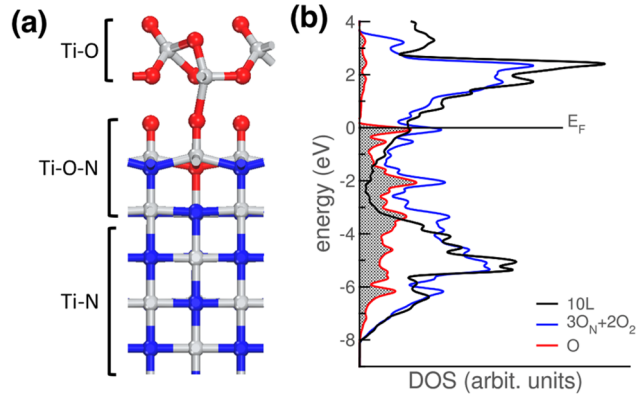

Figure 6. (a) Relaxed geometry of $3O_N + 2O_2$ configuration. (b) Total (blue line) and O-projected (shaded area) density of states of $3O_N + 2O_2$ configuration compared to the ideal unoxidized 10L case (black line). Zero energy reference is set to the Fermi level of the two systems.

condition (+6%) does not fit the experimental situation as the actual mismatch between TiN and MgO would result in a compressive strain of only ~0.7% (a_0^{MgO} = 4.21 Å). Thus, even though in principle strain may affect the optical properties of ultrathin films, in the present case oxidation seems to be the

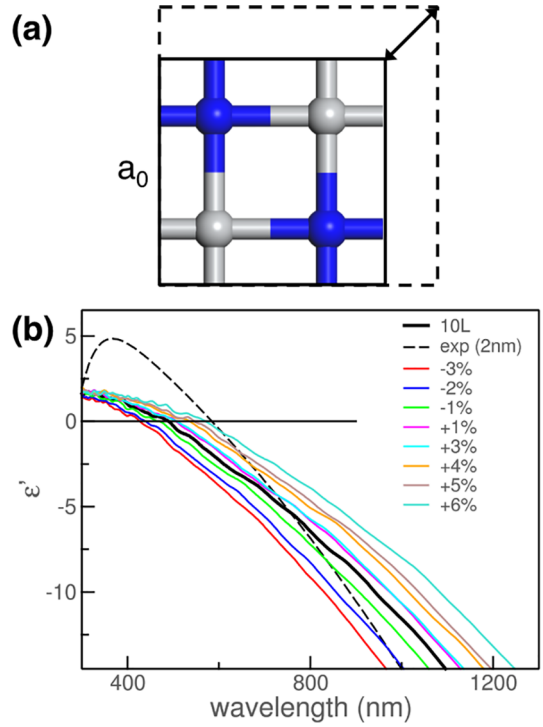

Figure 7. (a) In-plane strain model. (b) Simulated real part of the dielectric function for 10L TiN films, with varying amount of applied lateral strain. Theoretical ideal unstrained model (10L) and corresponding experimental spectra are reported in panel (b) for direct comparison.

most important cause of the differences between the ideal TiN model and measured sample with the same formal thickness.

To support these results, the substrate-induced strain is experimentally determined by high-angle annular dark field imaging scanning transmission electron microscopy (HAADF STEM) of a 2 nm TiN film grown on MgO, as shown in Figure 8. The observed contrast at the TiN/MgO interface signifies

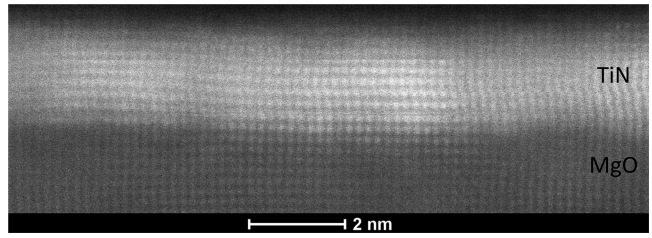

Figure 8. HAADF STEM image of a 2 nm TiN film on an MgO substrate. The contrast at the film/substrate interface is due to misfit dislocations, causing the film to relax.

the formation of misfit dislocations, indicating that the film has relaxed and has no substrate induced strain which may have influenced the optical properties. The strain relaxation mechanism is typically dependent on the growth process of the material. If the first few monolayers of TiN grown on MgO formed epitaxial islands having the same crystal orientation, the coalescence of the islands would create dislocations contributing to strain relaxation. Once the islands merge, a smooth, continuous, epitaxial film continues to grow.[59,60] This is consistent with the theoretical findings that the oxidation plays the main role in the difference between the simulations

DOI: 10.1021/acsphotonics.7b01553
ACS Photonics 2018, 5, 2816−2824

for pure TiN and experimental work. However, as the thickness decreases, the films may remain strained and exhibit a stronger effect on the changes in the optical properties.

Although MgO substrate does not to affect the position of λ_0, it acts as a dielectric environment that may change the optical response of TiN films at lower wavelengths (λ < 400 nm), that is, where ε' is positive and TiN acts as a dielectric medium. This is expected to be the cause of the enhancement of ε' experimental values compared to the theoretical ones (inset of Figure 2). This argument is in agreement with the results for TiN grown on c-sapphire (see SI for further details) as well as with the simplified theoretical model of the thin TiN/MgO interface, proposed in SI: The presence of the substrate increases the interband transitions in the UV range between substrate and film, which are responsible for the increase of the dielectric function. At odd, MgO does not alter the crossover wavelength of the film, which results strictly dependent on TiN thickness (see SI for further details).

The structural stability, the retention of the metallicity, and the tunability of the optical properties make ultrathin TiN films very promising candidates for nonlinear optics applications. Indeed, it has been demonstrated that, in ultrathin metallic films, the third order nonlinear susceptibility $\chi^{(3)}$ is greatly enhanced[15] due to contribution of transitions between electronic subbands, which derive from quantum confinement effect. The third order nonlinear susceptibility can be defined as[61] $\chi^{(3)} = \frac{n_e(\mu_{mn}^4)}{(\omega_{mn} - \omega - i\gamma_{mn})}$, where n_e is the carrier concentration, μ_{mn} is the dipole transition element between states n and m, and γ is the damping term. For intersubband transitions, the dipole transition elements μ_{mn} are in the range of a few nanometers rather than a few picometers, as it is in the case of bulk metals, giving an enhancement of $\chi^{(3)}$. In the case of ultrathin TiN films, this property along with the control of thickness and the high carrier density are expected to favor these nonlinear processes.

CONCLUSIONS

We have conducted a detailed theoretical and experimental study on the plasmonic behavior of ultrathin (down to a few atomic layers) TiN films to determine the role of thickness, surface oxidation and interface strain on TiN optical properties. As the thickness is reduced, the metallic character is also decreased as a result of quantum confinement effects, which increase the contribution from under-coordinated surface atoms leading to an increased electron localization. The atomistic analysis of the experimentally grown TiN thin films indicates a non-negligible deviation from the ideal TiN structure on the surface. We show that the fabricated films' composition can be described as a combination of three different phases: titanium nitride, titanium oxynitride, and titanium dioxide. The surface oxidation of the films, particularly affecting the Ti coordination, has a significant influence on the optical properties of the TiN films, which red shifts the crossover wavelength with respect to the ideal case with the same formal thickness. Additionally, although there is no strain observed in the current films studied, thinner films may exhibit a change in the lattice parameter, which would further affect the optical properties.

The investigated ultrathin films remain highly metallic and are characterized by plasmonic excitations in the visible wavelength range. More importantly, the fabricated ultrathin films' optical response can be adjusted by controlling their structural and compositional parameters, such as thickness, strain, and oxidation during growth. The observed plasmonic properties, in combination with the confinement effects, make TiN ultrathin films a promising material for the realization of plasmonic metasurfaces with enhanced nonlinearities and electrical tunability. Thus, ultrathin plasmonic TiN films can be profitably exploited in flexible (nonlinear) optoelectronics, for example, smart wearable or biomedical implantable devices.

ASSOCIATED CONTENT

Supporting Information

The Supporting Information is available free of charge on the ACS Publications website at DOI: 10.1021/acsphotonics.7b01553.

Details on theoretical characterization of TiN bulk, experimental characterization of ultrathin TiN films, description of ellipsometry and Hall measurements, and DFT results for TiN/MgO model interface (PDF).

AUTHOR INFORMATION

Corresponding Author

*E-mail: arrigo.calzolari@nano.cnr.it.

ORCID

Harsha Reddy: 0000-0003-3292-2221

Alexandra Boltasseva: 0000-0002-5988-7625

Arrigo Calzolari: 0000-0002-0244-7717

Author Contributions

D.S. and N.K. grew the TiN thin films. D.S. performed ellipsometry and analysis of XPS measurements of the thin films. H.R. conducted Hall measurements. V.S. and A.B. coordinated the experimental studies. A.C. performed DFT calculations. V.S., A.B, and A.C. conceived the project, analyzed the results, and contributed to write the paper.

Notes

The authors declare no competing financial interest.

ACKNOWLEDGMENTS

This work was supported from the NSF OP Grant DMR-1506775 and Air Force Office of Scientific Research MURI Grant (FA9550-14-1-0389). The authors would like to acknowledge Dr. Dmitry Zemlyanov for help with XPS characterization and Dr. Sergei Rouvimov for help with TEM characterization.

REFERENCES

(1) Kildishev, A. V.; Boltasseva, A.; Shalaev, V. M. Planar Photonics with Metasurfaces. *Science* **2013**, *339* (6125), 1232009.

(2) Anker, J. N.; Hall, W. P.; Lyandres, O.; Shah, N. C.; Zhao, J.; Van Duyne, R. P. Biosensing with Plasmonic Nanosensors. *Nat. Mater.* **2008**, *7* (6), 442−453.

(3) Rodrigo, D.; Limaj, O.; Janner, D.; Etezadi, D.; Abajo, F. J. G.; de Pruneri, V.; Altug, H. Mid-Infrared Plasmonic Biosensing with Graphene. *Science* **2015**, *349* (6244), 165−168.

(4) Mesch, M.; Metzger, B.; Hentschel, M.; Giessen, H. Nonlinear Plasmonic Sensing. *Nano Lett.* **2016**, *16* (5), 3155−3159.

(5) Atwater, H. A.; Polman, A. Plasmonics for Improved Photovoltaic Devices. *Nat. Mater.* **2010**, *9* (3), 205−213.

(6) Li, W.; Guler, U.; Kinsey, N.; Naik, G. V.; Boltasseva, A.; Guan, J.; Shalaev, V. M.; Kildishev, A. V. Refractory Plasmonics with Titanium Nitride: Broadband Metamaterial Absorber. *Adv. Mater.* **2014**, *26* (47), 7959−7965.

(7) Polman, A.; Atwater, H. A. Photonic design principles for ultrahigh-efficiency photovoltaics. *Nat. Mater.* **2012**, *11*, 174−177.

DOI: 10.1021/acsphotonics.7b01553
ACS Photonics 2018, 5, 2816−2824

(8) Kinsey, N.; Ferrera, M.; Naik, G. V.; Babicheva, V. E.; Shalaev, V. M.; Boltasseva, A. Experimental Demonstration of Titanium Nitride Plasmonic Interconnects. *Opt. Express* **2014**, *22* (10), 12238−12247.
(9) Gramotnev, D. K.; Bozhevolnyi, S. I. Plasmonics beyond the Diffraction Limit. *Nat. Photonics* **2010**, *4* (2), 83.
(10) Manjavacas, A.; Abajo, F. J. G. de. Tunable Plasmons in Atomically Thin Gold Nanodisks. *Nat. Commun.* **2014**, *5*, 3548.
(11) Shah, D.; Reddy, H.; Kinsey, N.; Shalaev, V. M.; Boltasseva, A. Optical Properties of Plasmonic Ultrathin TiN Films. *Adv. Opt. Mater.* **2017**, *5* (13), 1700065.
(12) Rivera, N.; Kaminer, I.; Zhen, B.; Joannopoulos, J. D.; Soljačić, M. Shrinking Light to Allow Forbidden Transitions on the Atomic Scale. *Science* **2016**, *353* (6296), 263−269.
(13) Özdemir, Ş. K.; Lee, J.; McEnery, K. R.; Kim, M. S.; Tame, M. S.; Maier, S. A. Quantum Plasmonics. *Nat. Phys.* **2013**, *9* (6), 329.
(14) Kinsey, N.; Syed, A. A.; Courtwright, D.; DeVault, C.; Bonner, C. E.; Gavrilenko, V. I.; Shalaev, V. M.; Hagan, D. J.; Stryland, E. W. V.; Boltasseva, A. Effective Third-Order Nonlinearities in Metallic Refractory Titanium Nitride Thin Films. *Opt. Mater. Express* **2015**, *5* (11), 2395−2403.
(15) Qian, H.; Xiao, Y.; Liu, Z. Giant Kerr Response of Ultrathin Gold Films from Quantum Size Effect. *Nat. Commun.* **2016**, *7*, 13153.
(16) Walsh, A.; Catlow, C. R. A.; Zhang, K. H. L.; Egdell, R. G. Control of the Band-Gap States of Metal Oxides by the Application of Epitaxial Strain: The Case of Indium Oxide. *Phys. Rev. B: Condens. Matter Mater. Phys.* **2011**, *83* (16), 161202.
(17) Bondarev, I. V.; Shalaev, V. M. Universal Features of the Optical Properties of Ultrathin Plasmonic Films. *Opt. Mater. Express* **2017**, *7* (10), 3731−3740.
(18) Lu, Y.-J.; Sokhoyan, R.; Cheng, W.-H.; Shirmanesh, G. K.; Davoyan, A. R.; Pala, R. A.; Thyagarajan, K.; Atwater, H. A. Dynamically Controlled Purcell Enhancement of Visible Spontaneous Emission in a Gated Plasmonic Heterostructure. *Nat. Commun.* **2017**, *8* (1), 1631.
(19) Kossoy, A.; Merk, V.; Simakov, D.; Leosson, K.; Kéna-Cohen, S.; Maier, S. A. Optical and Structural Properties of Ultra-Thin Gold Films. *Adv. Opt. Mater.* **2015**, *3* (1), 71−77.
(20) Van Bui, H.; Kovalgin, A. Y.; Wolters, R. A. M. On the Difference between Optically and Electrically Determined Resistivity of Ultra-Thin Titanium Nitride Films. *Appl. Surf. Sci.* **2013**, *269*, 45−49.
(21) Doron-Mor, I.; Barkay, Z.; Filip-Granit, N.; Vaskevich, A.; Rubinstein, I. Ultrathin Gold Island Films on Silanized Glass. Morphology and Optical Properties. *Chem. Mater.* **2004**, *16* (18), 3476−3483.
(22) Naik, G. V.; Saha, B.; Liu, J.; Saber, S. M.; Stach, E. A.; Irudayaraj, J. M. K.; Sands, T. D.; Shalaev, V. M.; Boltasseva, A. Epitaxial Superlattices with Titanium Nitride as a Plasmonic Component for Optical Hyperbolic Metamaterials. *Proc. Natl. Acad. Sci. U. S. A.* **2014**, *111* (21), 7546−7551.
(23) Naik, G. V.; Schroeder, J. L.; Ni, X.; Kildishev, A. V.; Sands, T. D.; Boltasseva, A. Titanium Nitride as a Plasmonic Material for Visible and Near-Infrared Wavelengths. *Opt. Mater. Express* **2012**, *2* (4), 478.
(24) Patsalas, P.; Kalfagiannis, N.; Kassavetis, S. Optical Properties and Plasmonic Performance of Titanium Nitride. *Materials* **2015**, *8* (6), 3128−3154.
(25) Matenoglou, G. M.; Lekka, C. E.; Koutsokeras, L. E.; Karras, G.; Kosmidis, C.; Evangelakis, G. A.; Patsalas, P. Structure and Electronic Properties of Conducting, Ternary $Ti_xTa_{1-x}N$ Films. *J. Appl. Phys.* **2009**, *105* (10), 103714.
(26) Ern, V.; Switendick, Ac. Electronic Band Structure of TiC, TiN, and TiO. *Phys. Rev.* **1965**, *137* (6A), 1927.
(27) Pearson, W. B. Structure Reports: TiN. *Oosthoek, Scheltema and Holkema for International Union of Crystallography*; Uitgevers Mij. N.V., 1993; Vol. *11*.
(28) Gubanov, V. A.; Ivanovsky, A. L.; Zhukov, V. P. *Electronic Structure of Refractory Carbides and Nitrides*; Cambridge University Press: Cambridge, 1994.
(29) Patsalas, P.; Charitidis, C.; Logothetidis, S. In Situ and Real-Time Ellipsometry Monitoring of Submicron Titanium Nitride Titanium Silicide Electronic DevicesElectronic Structure of Refractory Carbides and Nitrides. *Appl. Surf. Sci.* **2000**, *154−155*, 256−262.
(30) Langereis, E.; Heil, S. B. S.; Knoops, H. C. M.; Keuning, W.; van de Sanden, M. C. M.; Kessels, W. M. M. In Situ Spectroscopic Ellipsometry as a Versatile Tool for Studying Atomic Layer Deposition. *J. Phys. D: Appl. Phys.* **2009**, *42*, 073001.
(31) Höchst, H.; Bringans, R. D.; Steiner, P.; Wolf, Th. Photoemission Study of the Electronic Structure of Stoichiometric and Substoichiometric TiN and ZrN. *Phys. Rev. B: Condens. Matter Mater. Phys.* **1982**, *25*, 7183−7191.
(32) Walker, C. G. H.; Anderson, C. A.; McKinley, A.; Brown, N. M. D.; Joyce, A. M. A Combined AES, Resonant Photoemission and EELS Study of in-Situ Grown Titanium Nitride. *Surf. Sci.* **1997**, *383*, 254−260.
(33) Pflüger, J.; Fink, J.; Weber, W.; Bohnen, K. P.; Crecelius, G. Dielectric Properties of TiC_x, TiN_x, VC_x, and VN_x from 1.5 to 40 EV Determined by Electron-Energy-Loss Spectroscopy. *Phys. Rev. B: Condens. Matter Mater. Phys.* **1984**, *30* (3), 1155−1163.
(34) Herzing, A. A.; Guler, U.; Zhou, X.; Boltasseva, A.; Shalaev, V. M.; Norris, T. B. Electron Energy Loss Spectroscopy of Plasmon Resonances in Titanium Nitride Thin Films. *Appl. Phys. Lett.* **2016**, *108*, 171107.
(35) Gall, D.; Petrov, I.; Greene, J. E. Epitaxial $Sc_{1-x}Ti_xN(001)$: Optical and Electronic Transport Properties. *J. Appl. Phys.* **2001**, *89*, 401−409.
(36) Chou, W. J.; Yu, G. P.; Huan, J. H. Mechanical Properties of TiN Thin Film Coatings on 304 Stainless Steel Substrates. *Surf. Coat. Technol.* **2002**, *149*, 7−13.
(37) Fayeulle, S.; Ehni, P. D. Friction and Wear Behavior of TiN in Air: The Chemistry of Transfer Films and Debris Formation. *Wear* **1991**, *149*, 375−394.
(38) Margine, E. R.; Kolmogorov, A. N.; Reese, M.; Mrovec, M.; Elsässer, C.; Meyer, B.; Drautz, R.; Pettifor, D. G. Development of Orthogonal Tight-Binding Models for Ti-C and Ti-N Systems. *Phys. Rev. B: Condens. Matter Mater. Phys.* **2011**, *84*, 155120.
(39) Delin, A.; Eriksson, O.; Ahuja, R.; Johansson, B.; Brooks, M. S. S.; Gasche, T.; Auluck, S.; Wills, J. M. Optical Properties of the Group-IVB Refractory Metal Compounds. *Phys. Rev. B: Condens. Matter Mater. Phys.* **1996**, *54*, 1673.
(40) Catellani, A.; Calzolari, A. Plasmonic Properties of Refractory Titanium Nitride. *Phys. Rev. B: Condens. Matter Mater. Phys.* **2017**, *95* (11), 115145.
(41) Ingason, A. S.; Magnus, F.; Agustsson, J. S.; Olafsson, S.; Gudmundsson, J. T. In-Situ Electrical Characterization of Ultrathin TiN Films Grown by Reactive Dc Magnetron Sputtering on SiO_2. *Thin Solid Films* **2009**, *517*, 6731−6736.
(42) Kroger, R.; Eizenberg, M.; Marcadal, C.; Chen, L. Plasma Induced Microstructural, Compositional, and Resistivity Changes in Ultrathin Chemical Vapor Deposited Titanium Nitride Films. *J. Appl. Phys.* **2002**, *91*, 5149.
(43) Chawla, J. S.; Zhang, X. Y.; Gall, D. Effective Electron Mean Free Path in TiN(001). *J. Appl. Phys.* **2013**, *113*, 063704.
(44) Van Bui, H.; Kovalgin, A. J.; Schmitz, J.; Wolters, R. A. M. Conduction and Electric Field Effect in Ultra-Thin TiN Films. *Appl. Phys. Lett.* **2013**, *103*, 051904.
(45) Perdew, J. P.; Burke, K.; Ernzerhof, M. Generalized Gradient Approximation Made Simple. *Phys. Rev. Lett.* **1996**, *77* (18), 3865−3868.
(46) Troullier, N.; Martins, J. L. Efficient Pseudopotentials for Plane-Wave Calculations. *Phys. Rev. B: Condens. Matter Mater. Phys.* **1991**, *43* (3), 1993−2006.
(47) Giannozzi, P.; Baroni, S.; Bonini, N.; Calandra, M.; Car, R.; Cavazzoni, C.; Ceresoli, D.; Chiarotti, G. L.; Cococcioni, M.; Dabo, I.; et al. QUANTUM ESPRESSO: A Modular and Open-Source Software Project for Quantum Simulations of Materials. *J. Phys.: Condens. Matter* **2009**, *21* (39), 395502.

DOI: 10.1021/acsphotonics.7b01553
ACS Photonics 2018, 5, 2816−2824

(48) Colle, R.; Parruccini, P.; Benassi, A.; Cavazzoni, C. Optical Properties of Emeraldine Salt Polymers from Ab Initio Calculations: Comparison with Recent Experimental Data. *J. Phys. Chem. B* **2007**, *111* (11), 2800−2805.
(49) Calzolari, A.; Ruini, A.; Catellani, A. Transparent Conductive Oxides as Near-IR Plasmonic Materials: The Case of Al-Doped ZnO Derivatives. *ACS Photonics* **2014**, *1* (8), 703−709.
(50) Eaton, M.; Catellani, A.; Calzolari, A. VO_2 as a Natural Optical Metamaterial. *Opt. Express* **2018**, *26*, 5342−5357.
(51) Campione, S.; Brener, I.; Marquier, F. Theory of Epsilon-near-Zero Modes in Ultrathin Films. *Phys. Rev. B: Condens. Matter Mater. Phys.* **2015**, *91* (12), 121408.
(52) Vassant, S.; Hugonin, J.-P.; Marquier, F.; Greffet, J.-J. Berreman Mode and Epsilon near Zero Mode. *Opt. Express* **2012**, *20* (21), 23971−23977.
(53) Guler, U.; Suslov, S.; Kildishev, A. V.; Boltasseva, A.; Shalaev, V. M. Colloidal Plasmonic Titanium Nitride Nanoparticles: Properties and Applications. *Nanophotonics* **2015**, *4* (3), 269−276.
(54) Milošv, I.; Strehblow, H.-H.; Navinšek, B.; Metikoš-Huković, M. Electrochemical and Thermal Oxidation of TiN Coatings Studied by XPS. *Surf. Interface Anal.* **1995**, *23* (7−8), 529−539.
(55) Zgrabik, C. M.; Hu, E. L. Optimization of Sputtered Titanium Nitride as a Tunable Metal for Plasmonic Applications. *Opt. Mater. Express* **2015**, *5* (12), 2786−2797.
(56) Jiang, N.; Zhang, H. J.; Bao, S. N.; Shen, Y. G.; Zhou, Z. F. XPS Study for Reactively Sputtered Titanium Nitride Thin Films Deposited under Different Substrate Bias. *Phys. B* **2004**, *352* (1), 118−126.
(57) Cheng, Y.; Zheng, Y. F. Surface Characterization and Mechanical Property of TiN/Ti-Coated NiTi Alloy by PIIID. *Surf. Coat. Technol.* **2007**, *201* (15), 6869−6873.
(58) Braic, L.; Vasilantonakis, N.; Mihai, A.; Villar Garcia, I. J.; Fearn, S.; Zou, B.; Alford, N. M.; Doiron, B.; Oulton, R. F.; Maier, S. A.; et al. Titanium Oxynitride Thin Films with Tunable Double Epsilon-Near-Zero Behavior for Nanophotonic Applications. *ACS Appl. Mater. Interfaces* **2017**, *9* (35), 29857−29862.
(59) Magnus, F.; Ingason, A. S.; Olafsson, S.; Gudmundsson, J. T. Growth and In-Situ Electrical Characterization of Ultrathin Epitaxial TiN Films on MgO. *Thin Solid Films* **2011**, *519* (18), 5861−5867.
(60) King, D. A.; Woodruff, D. P. *Growth and Properties of Ultrathin Epitaxial Layers*; Elsevier: Burlington, 1997.
(61) Boyd, R. W. *Nonlinear Opt.*; Elsevier, 2008.

DOI: 10.1021/acsphotonics.7b01553
ACS Photonics 2018, 5, 2816−2824

SUPPORTING INFORMATION FOR

Controlling the plasmonic properties of ultrathin TiN films at the atomic level

*Deesha Shah, Alessandra Catellani, Harsha Reddy, Nathaniel Kinsey, Vladimir M. Shalaev, Alexandra Boltasseva, Arrigo Calzolari**

[1] School of Electrical and Computer Engineering and Birck Nanotechnology Center, Purdue University, West Lafayette, Indiana 47907, USA
[2] CNR-NANO Istituto Nanoscienze, Centro S3, I-41125 Modena, IT
[3] School of Electrical and Computer Engineering, Virginia Commonwealth University, Richmond, Virginia 23220, USA

S1. TiN Bulk

Figure S1 shows the complex dielectric function of TiN bulk in the rocksalt B_1 phase, calculated with the independent particle (IP) approach based on the Drude-Lorentz model used in this work (Eq. 1, main text) and with Time-Dependent Density Functional Perturbation Theory (TD-DFPT) [S1] implemented for the evaluation of **q**-dependent EELS spectra in the limit for transferred momentum $q \rightarrow 0$. The two spectra are identical, within the numerical errors. See Ref [S2] for further details and comparison with experiments and previous theoretical data.

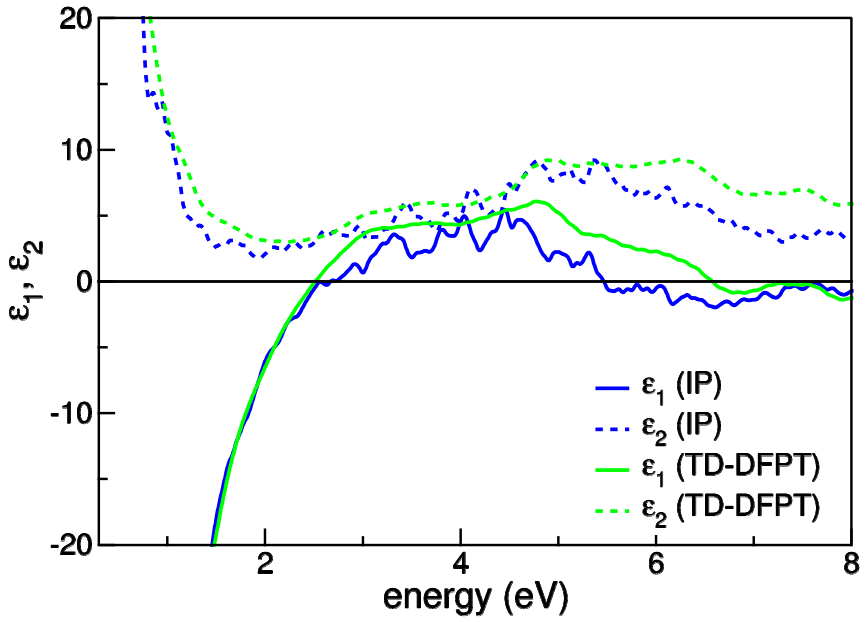

Figure S1. Complex dielectric function of TiN bulk, calculated with IP and TD-DFPT approaches.

S2. TiN films – experimental characterization

The complete experimental characterization of ultrathin TiN films is reported elsewhere [S3]. Here we summarize (Figure S2) the most relevant experimental data, discussed in the main text. Panel (a) reports the carrier charge density as retrieved from Hall measurements and panel (b) the real part of the dielectric function of resulting from ellipsometry measurements. Spectra for thick films (100 nm) from present work and from Patsalas et al. [S4] are included in panel (b) for comparison. The permittivity reported by Patsalas et al. (dashed line) matches well with present experimental results. The discrepancies may be attributed to variations in the crystallinity and film quality as a result of different growth processes and substrate. The films fabricated by Patsalas et al. are grown on silicon at room temperature with a voltage bias resulting in polycrystalline films, while our films are grown on MgO at 800 °C resulting in epitaxial films.

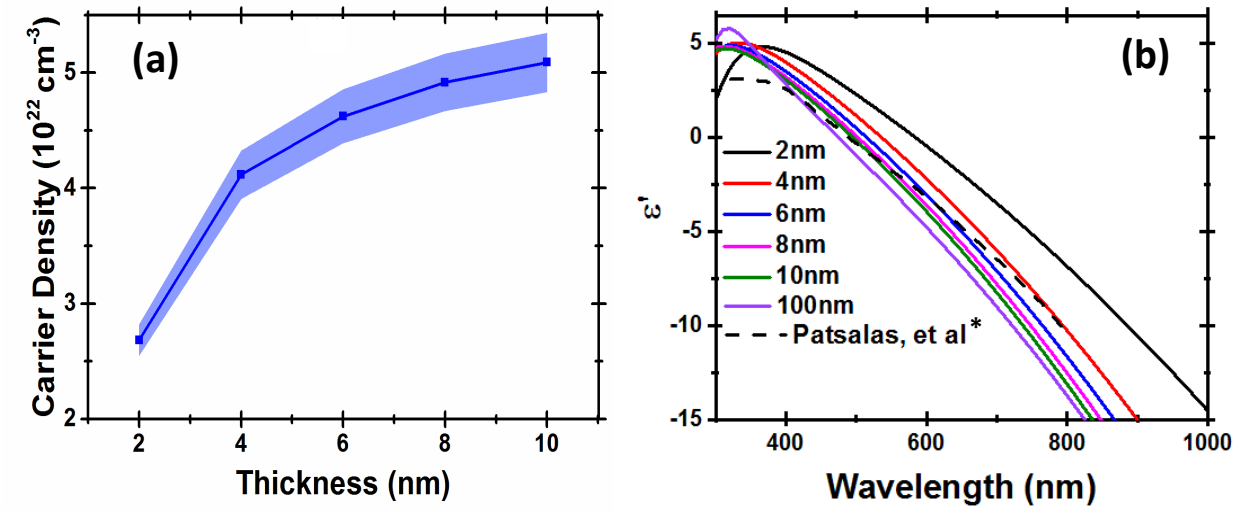

Figure S2. Charge density obtained from Hall measurements and (b) real part of the dielectric function from ellipsometry measurements for increasing TiN film thicknesses.
* Experimental set adapted from Ref. [S4].

S3. E_0 vs number of layers

In order to extrapolate the limit for films of increasing thickness, we plot (Figure S3) the screened plasmon energy E_0 as a function of $1/N_L$, where N_L is the number of layers in the simulated system. Two distinct regimes are clearly evident: one dominated by quantum confinement effect for very thin films (1-3 layers, open red circle), one (filled circles) for thicker films. This indicates that trends from theoretical results are meaningful for comparison with experimental data even for thicker films.

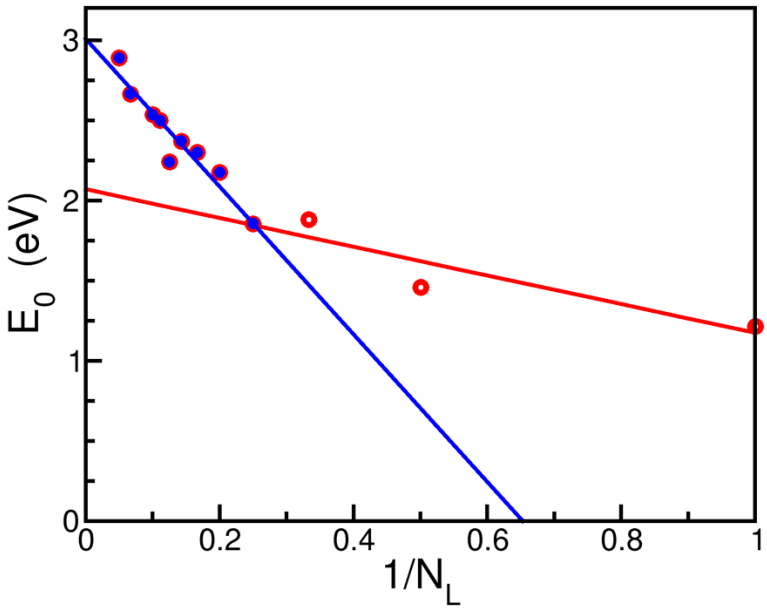

Figure S3. Screened plasmon energy E_0 as a function of the number of TiN(100) layers (N_L).

S3. Ellipsometry Measurements

In spectroscopic ellipsometry, a linearly polarized light is incident on a substrate at an oblique angle. The relative changes in the amplitude, Ψ, and the phase difference, Δ, of the light reflected off the substrate are measured and related to the Fresnel reflection coefficients as,

$$\rho = \frac{R_p}{R_s} = \tan(\Psi)\, e^{i\Delta}$$

where R_p and R_s are the Fresnel reflection coefficients for p-polarized and s-polarized light respectively. Figure S4 shows the measured Ψ and Δ values for angles of 50° and 70°.

The optical constants are determined by fitting the measured data using a Drude – Lorentz model:

$$\varepsilon(E) = \varepsilon_b - \frac{A_0}{E^2 + iB_0E} + \sum_n \frac{A_n}{E_n^2 - E^2 - iB_nE}$$

where A_n is the amplitude, E_n is the center energy of the Lorentz oscillator and B_n is the broadening of each oscillator. The dielectric function of the substrate obtained from ellipsometry that is used in the fittings is shown in Figure S5. Since the dielectric functions of the ultra-thin TiN films are heavily dependent on the thickness in this regime, the thickness is kept fixed to the target thickness for the ellipsometry fittings. Table S1 provides the fit parameters for the films studied.

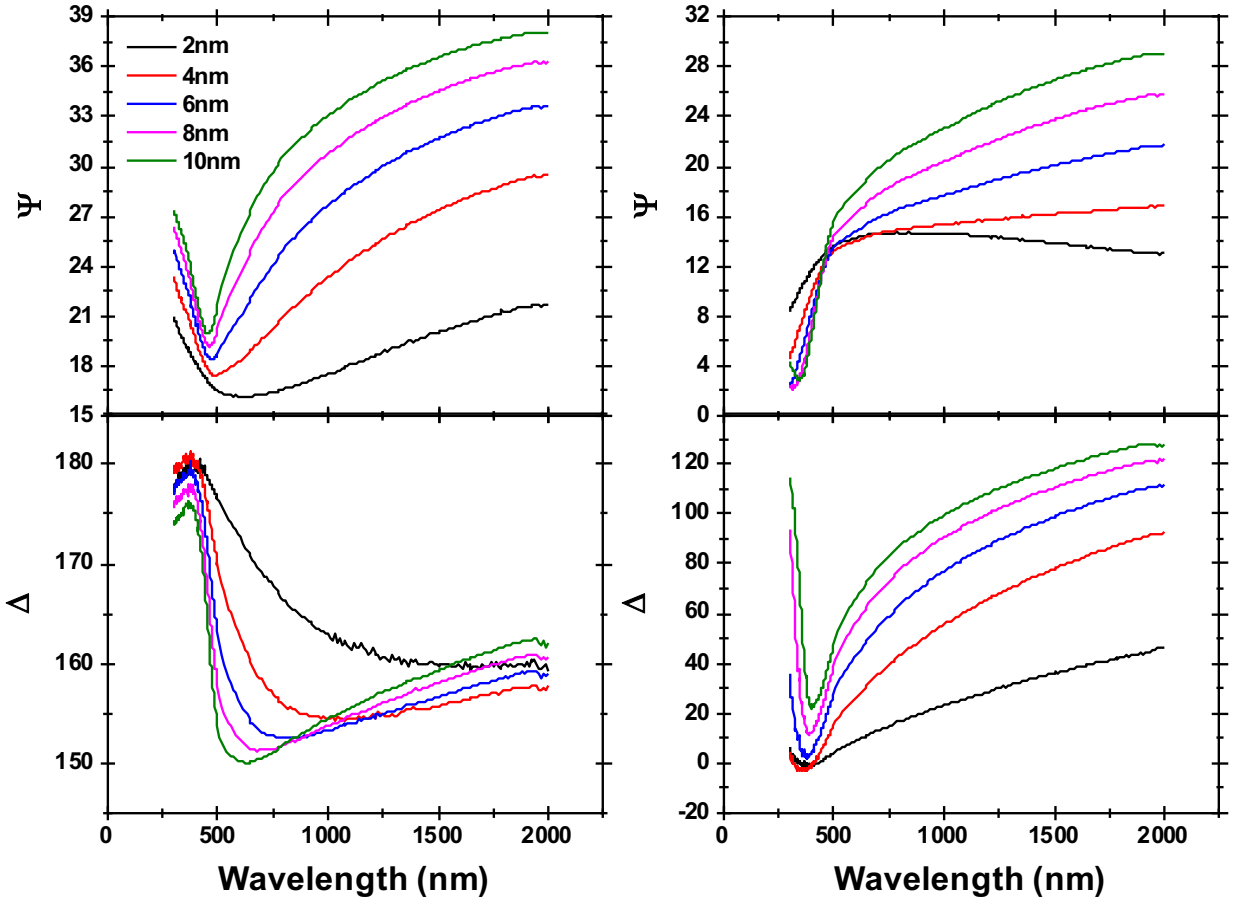

Figure S4. Ellipsometry measurements, Ψ and Δ, of the ultrathin films. (a) and (c) are Ψ and Δ for 50°, while (b) and (d) are Ψ and Δ for 70°.

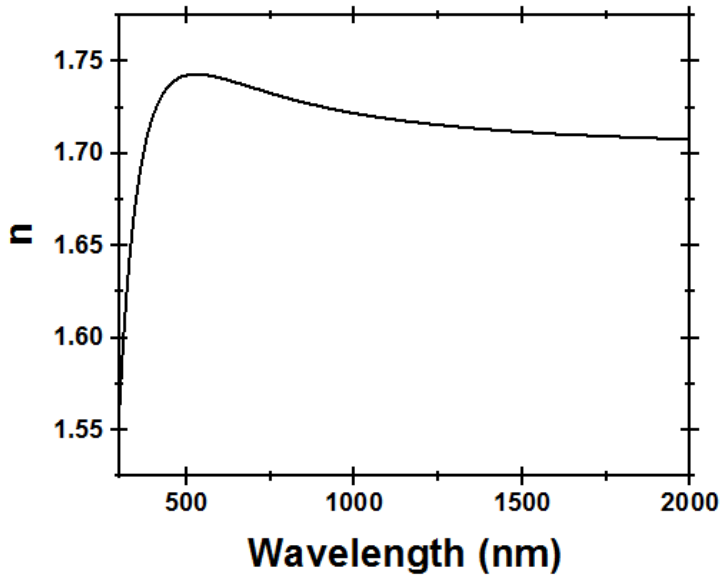

Figure S5. The refractive index of an MgO substrate as retrieved from ellipsometry.

Table S1. Fitted parameters using a Drude-Lorentz model. MSE is the mean square error of the fittings.

	Thickness (nm)				
	2	**4**	**6**	**8**	**10**
ε_b	0.92	2.66	2.95	3.11	3.28
A_0 **(eV)**^{2}	34.98	44.97	48.2	50.2	51.66
B_0 **(eV)**	0.282	0.247	0.236	0.232	0.229
E_0 **(eV)**	0	0	0	0	0
A_2 **(eV)**^{2}	0.28	0.58	0.7	0.68	0.72
B_2 **(eV)**	0.35	0.45	0.5	0.49	0.53
E_2 **(eV)**	2.15	2.16	2.18	2.19	2.16
A_3 **(eV)**^{2}	113.9	105.2	100.1	99.6	96.7
B_3 **(eV)**	2.38	2.48	2.47	2.54	2.53
E_3 **(eV)**	4.44	4.65	4.7	4.78	4.79
MSE	1.7	2.08	3.3	4.5	5.6

S.4 Resistivity Measurements

The resistivity measured from the optical and electrical characterizations are compared. The optical resistivity of the films is extracted from the Drude damping factor obtained from the ellipsometry measurements, as

$$\rho = \frac{\Gamma}{\varepsilon_0 \omega_p^2}$$

where Γ is the Drude damping and ω_p is the plasma frequency. The electrical resistivity is measured using the four-point probe method on the ultra-thin films.

For both the electrical and optical measurements, the resistivity increases in thinner films. Differences in the measured data may be attributed to how the scattering effects contribute to the resistivity calculations in each technique. In ellipsometry, the scattering originates from the electrons' interaction with light. On the other hand, electrical measurements depend on the scattering during the electron's path from one electrode to another.

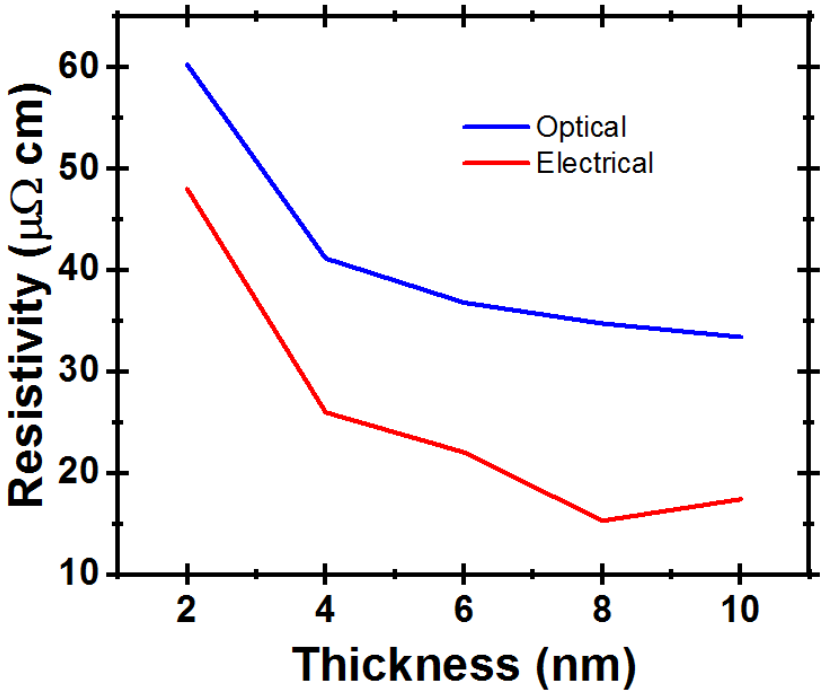

Figure S6. Optical and electrical resistivity retrieved from ellipsometry and four point probe measurements respectively

S5. Effect of MgO substrate

In the experimental spectra of Figure S2b (ellipsometry measurements), we detect a local maximum at ~400nm, which is characteristic only of the 2nm and 4nm films. In the thicker films, the local maximum appears at a lower wavelength (~320nm). This is consistent with other experimental and theoretical reports for bulk TiN. At smaller thicknesses, the substrate has a more pronounced effect on the permittivity of the films [S5], which is most probably due to a dielectric effect from the substrate. The same maximum is also present in films grown on c-sapphire, which has a comparable refractive index to MgO (Figure S7).

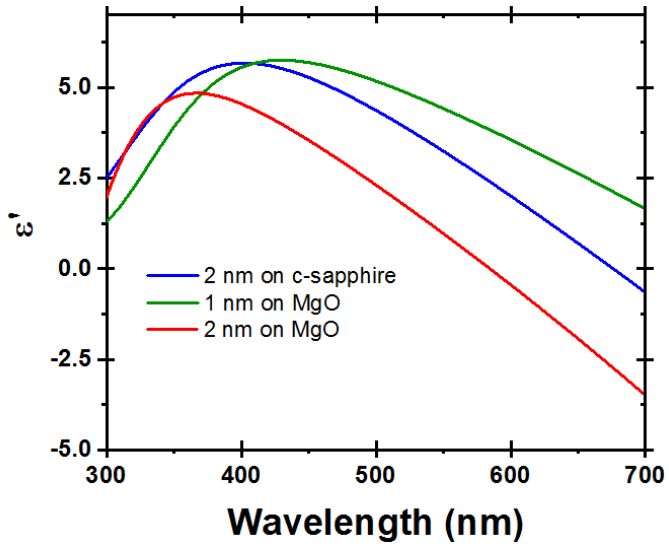

Figure S7. Real part of the dielectric function from ellipsometry measurements for ultrathin TiN films grown on MgO and c-sapphire substrate.

In order to give a *qualitative* characterization of the screening effect of MgO substrate on TiN dielectric properties, we calculated the optical properties of a thin TiN/MgO interface. Since TiN and MgO are almost lattice matched, we fixed the lateral periodicity to TiN lattice parameter. The simulation cell, (4.24 x 4.24 x 55.00) $Å^3$, includes 5 layers (1nm) of TiN(100) and 10 layers (2nm) of MgO(100), as shown in Figure S8a. In order to correct the well-known bandgap underestimation of standard DFT, we adopted a recent pseudohybrid Hubbard implementation of DFT+U (namely ACBN0 approach [S6]) that profitably corrects the energy bandgap, and the dielectric and vibrational properties of semiconductors [S6]. The U values for Mg and O resulting from ACBN0 cycle and used for the calculations are: U_{3s}(Mg)= 0.52 eV and U_{2p}(O)=8.30 eV, respectively. The resulting band gap for MgO bulk is E_g=7.46 eV (E_g^{exp}=7.8eV) and the dielectric constant ε^{∞}=1.8 ($\varepsilon^{\infty}_{exp}$=2.9).

Optical properties of TiN/MgO interface are summarized in Figure S8b, which shows the real part of the dielectric function (black line), where we superimposed the results for *free standing* 1nm-TiN (5L, turquoise line) and 3nm-TiN (15L, orange line), for comparison.

Albeit 2nm-thickness is certainly too small to fully reproduce the overall dielectric properties of the MgO substrate, Figure S8 underlines interesting issues: (1) the inclusion of the substrate increases the dielectric response of the system in the UV region of the spectrum, which is due to an enhancement of the joint density of states (not-shown) deriving from TiN → MgO interband transitions (see DOS superposition in panel c). (2) MgO does not affect the position of the crossover wavelength, which recovers the same value of free standing 1nm-TiN. (3) The blue shift of crossover frequency as the thickness is increased is mainly associated to the thickness of TiN films and not to the overall interface (i.e. to the substrate). (4) The present model reproduces a perfect interface between perfectly matched surfaces. In this case Ti atoms at the interface maintain their original coordination and do not exhibit the red-shift behavior due to oxynitride compounds, addressed in the main text.

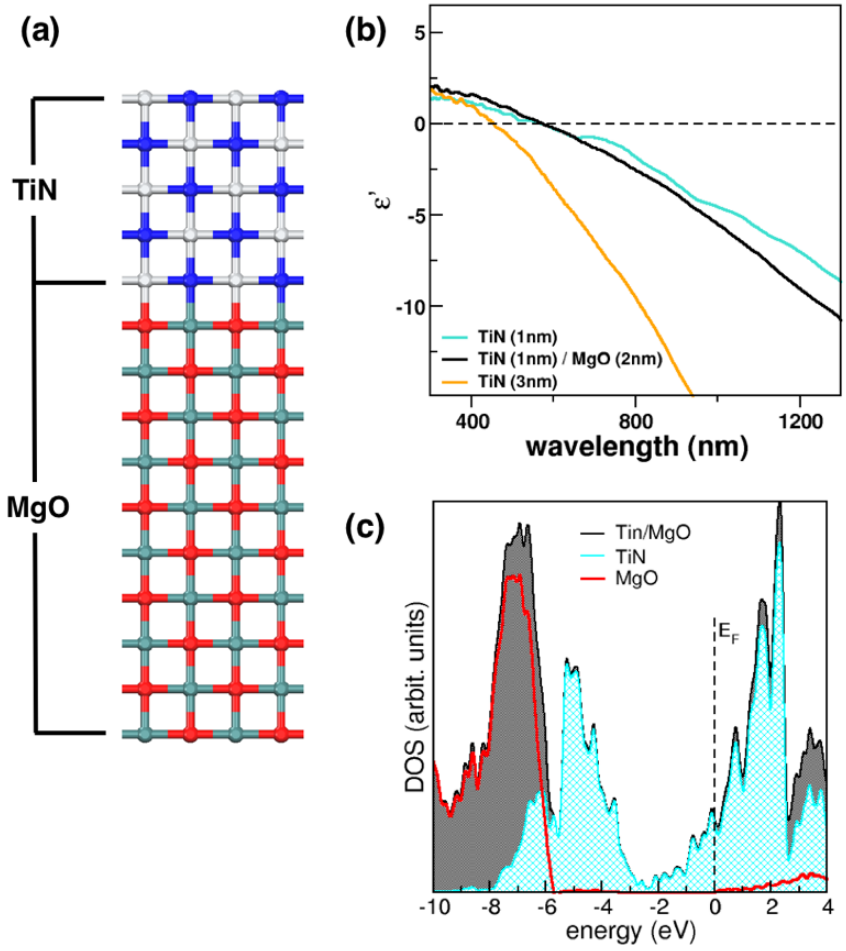

Figure S8. Simulated TiN/MgO interface: a) atomic structure (side view); b) real part of the dielectric function; c) total (black area) and TiN- (cyan area) and MgO-projected (red line) density of state. Vertical dashed line marks the Fermi Level (E_F) of the interface.

References

[S1] Timrov, I.; Vast, N.; Gebauer, R.; Baroni, S., Electron energy loss and inelastic x-ray scattering cross sections from time-dependent density-functional perturbation theory, *Phys. Rev. B* **2013**, *88*, 064301.

[S2] Catellani, A.; Calzolari, A. Plasmonic Properties of Refractory Titanium Nitride. *Phys. Rev. B* **2017**, *95* (11), 115145.

[S3] Shah, D.; Reddy, H.; Kinsey, N.; Shalaev, V. M.; Boltasseva, A. Optical Properties of Plasmonic Ultrathin TiN Films. *Advanced Optical Materials* **2017**, *5* (13), 1700065 (1-5).

[S4] Patsalas, P.; Kalfagiannis, N.; Kassavetis, S. Optical Properties and Plasmonic Performance of Titanium Nitride. *Materials* **2015***, 8* (6), 3128–3154.

[S5] Bondarev, I. V.; Shalaev, V. M. Universal Features of the Optical Properties of Ultrathin Plasmonic Films. *Opt. Mater. Express*, **2017**, *7* (10), 3731–3740.

[S6] (a) Agapito, L. A.; Curtarolo, S.; Buongiorno Nardelli, M. Reformulation of DFT + U as a pseudohybrid hubbard density functional for accelerated materials discovery, *Phys. Rev. X,* **2015***, 5*, 1–16; (b) Gopal, P.; Fornari, M.; Curtarolo, S.; Agapito, L. A.; Liyanage, L. S. I.; Buongiorno Nardelli, M. Improved predictions of the physical properties of Zn- and Cd-based wide band-gap semiconductors: A validation of the ACBN0 functional, *Phys. Rev. B,* **2015***, 91*, 245202–9.